Journal of Sound and Vibration 332 (2013) 1465–1483

Contents lists available at SciVerse ScienceDirect

Journal of Sound and Vibration

journal homepage: www.elsevier.com/locate/jsvi

Nonlinear dynamic vibration absorbers with a saturation

M. Febbo [a,*], S.P. Machado [b,c]

[a] Instituto de Física del Sur (IFISUR), Consejo Nacional de Investigaciones Científicas y Técnicas (CONICET) and Departamento de Física, Universidad Nacional del Sur (UNS), Av Alem 1253, 8000 Bahía Blanca, Argentina

[b] Grupo de Análisis de sistemas mecánicos, Centro de Investigaciones de Mecánica Teórica y Aplicada, Universidad Tecnológica Nacional FRBB, 11 de Abril 461, 8000 Bahía Blanca, Argentina

[c] Consejo Nacional de Investigaciones Científicas y Técnicas (CONICET), Argentina

ARTICLE INFO

Article history:
Received 23 April 2012
Received in revised form
21 November 2012
Accepted 22 November 2012
Handling Editor: Ivana Kovacic

ABSTRACT

The behavior of a new type of nonlinear dynamic vibration absorber is studied. A distinctive characteristic of the proposed absorber is the impossibility to extend the system to infinity. The mathematical formulation is based on a finite extensibility nonlinear elastic potential to model the saturable nonlinearity. The absorber is attached to a single degree-of-freedom linear/nonlinear oscillator subjected to a periodic external excitation. In order to solve the equations of motion and to analyze the frequency-response curves, the method of averaging is used. The performance of the FENE absorber is evaluated considering a variation of the nonlinearity of the primary system, the damping and the linearized frequency of the absorber and the mass ratio. The numerical results show that the proposed absorber has a very good efficiency when the nonlinearity of the primary system increases. When compared with a cubic nonlinear absorber, for a large nonlinearity of the primary system, the FENE absorber shows a better effectiveness for the whole studied frequency range. A complete absence of quasi-periodic oscillations is also found for an appropriate selection of the parameters of the absorber. Finally, direct integrations of the equations of motion are performed to verify the accuracy of the proposed method.

1. Introduction

Linear dynamic vibration absorbers have been proven to be a very effective and efficient way to mitigate undesirable vibration levels at certain (resonance) frequencies. Since the pioneering work of Frahm in 1909 [1] a large number of papers has been devoted to studying, improving and testing these relatively simple devices in vibration suppression and isolation. The theory of the linear vibration absorber is well documented in the literature [2,3] and is still a field of very active research [4]. Nevertheless, most of these linear absorbers are efficient only over a very narrow band of excitation frequencies. To overcome this, some researches started to study absorbers with nonlinear or piecewise linear characteristics [5,6]. Examples of this can be observed in several studies on nonlinear dynamic vibration absorbers (NDVAs) or nonlinear tuned mass dampers which have been carried out from the second half of the last century onwards. It is worth mentioning the works of Robertson [7], Pipes [8], Soom and Lee [9] and Nissen et. al. [10]. The aim of their works was to optimize these devices for vibration reduction either by maximizing the suppression bandwidth

* Corresponding author.
E-mail address: mfebbo@uns.edu.ar (M. Febbo).

0022-460X/$ - see front matter
http://dx.doi.org/10.1016/j.jsv.2012.11.025

or minimizing the maximum displacement of the main system. By applying several approximation methods, such as the Ritz method or the Harmonic Balance Method they could calculate the steady-state responses. More recently, the works by Rice [11] and Shaw et al. [12] extended those first reports pointing out that there is possibility of a combination instability in the suppression region if damping is kept slow. They studied under which circumstances this occurs, observing the coexistence of almost-periodic motion (due to Hopf bifurcations) and low-amplitude steady-state responses. Natsiavas [13] further studied this phenomenon, indicating that a proper selection of the system parameters can avoid this instability which can lead to dangerous effects. Oueini et al. [14] presented an approach for implementing an active nonlinear vibration absorber for flexible structures that exploited the saturation phenomenon exhibited by multi-degree-of-freedom systems with quadratic nonlinearities. And in a second work [15], they studied the dynamics of a nonlinear active vibration absorber with cubic nonlinearities. The nonlinear dynamics of a two-degree-of-freedom system with nonlinear damping and nonlinear spring were presented by Zhu et al. [16] with the aim of studying the effect of the nonlinear damping in the steady-state response of a cubic NDVA. Also Alexander et al. presented two interesting theoretical and experimental works [5,17] that explored the performance of a NDVA of cubic type in seismic isolation, and the theoretical effects of energy pumping with external excitation. Targeted energy transfer (TET) in two degree-of-freedom systems comprising a linear primary system and a nonlinear attachment has received a lot of attention in the field of vibration control [18]. It was demonstrated that at certain ranges of parameters and initial conditions, passive TET makes it possible that vibration energy initially localized in the linear oscillator gets passively transferred to the attachment in an almost irreversible way [19]. Most of these models consider a stiff nonlinear cubic spring and a linear damper attached to the primary system, but recently the use of nonlinear attachments with non-polynomial characteristics has also been studied [20].

The aim of the present work is to present a new type of NDVA. It consists of a strong nonlinear oscillator with a saturable nonlinearity which physically represents the impossibility to extend the system to infinity. The saturable nonlinearity is modeled by a finite extensibility nonlinear elastic (FENE) potential, which has been previously studied by one of the authors [21,22]. Additionally, some other authors [23,24] explored analytically and experimentally oscillators with a similar type of saturable nonlinearity constructed from a negative stiffness mechanism for vibration isolation purposes. The proposed NDVA is studied by coupling it to a harmonically driven linear/nonlinear oscillator (primary system) to analyze its efficiency in mitigating the vibration amplitude of the primary system. It is expected that the proposed NDVA presents a great efficiency for a strong nonlinear primary system. After an introductory section, Section 2 introduces the mathematical formulation of the problem. The following section (Section 3) presents the frequency-response curve (FRC) for the steady-state response of the compound system. Section 4 presents the numerical results and analyzes the FRCs in various cases. First we vary the degree of nonlinearity of the primary system in order to test the efficiency of the FENE absorber (Section 4.1). Then we conduct a variation of the main parameters of the absorber: damping ratio (Section 4.2.1), linearized frequency (Section 4.2.2)) and mass ratio (Section 4.2.3) to obtain a complete characterization with the idea of a future optimization of its parameters. In order to compare the efficiency of the proposed device with other well-known nonlinear absorbers [13], we perform a direct comparison with a cubic absorber in Section 4.3. Finally, Section 4.4 presents a direct numerical integration of the equations of motion to test the accuracy of the proposed approximate solution. Concluding remarks are then presented and discussed in Section 5.

2. Mathematical model

The FENE potential is used in this work to model the saturable nonlinearity of the absorber which physically represents the finite extensibility of the attached system. Mathematically, it is given by the following expression:

$$V_{\mathrm{FENE}}(x) = -\frac{1}{2}k_F \ln\left(1-\left(\frac{x}{x_0}\right)^2\right) \tag{1}$$

Consequently, the force is given by

$$f_{\mathrm{FENE}}(x) = -\frac{\mathrm{d}V_{\mathrm{FENE}}(x)}{\mathrm{d}x} = k_F \frac{x}{1-\left(\dfrac{x}{x_0}\right)^2} \tag{2}$$

where x represents the amplitude of the oscillator and x_0 its maximum possible extension. The system studied is modeled as a two-degree-of-freedom oscillator. A mechanical model of this system can be observed in Fig. 1. We consider a single degree-of-freedom nonlinear cubic oscillator of mass m_1 as the primary system. It is attached to a rigid boundary through a linear viscous damper and a linear/nonlinear spring on the left side and with a FENE oscillator (absorber) on the right side. As stated in the Introduction, the finite extensibility nonlinear oscillator acts as a dynamic vibration absorber of nonlinear characteristics. The two equations of motion, which result after applying Newton's second law, can be written as

$$m_1\ddot{x}_1 + c_1\dot{x}_1 + k_1x_1 + k_{1\mathrm{NL}}x_1^3 - k_{2F}\frac{(x_2-x_1)}{1-\left(\dfrac{x_2-x_1}{x_0}\right)^2} - c_2(\dot{x}_2-\dot{x}_1) = f\cos(\omega t) \tag{3}$$

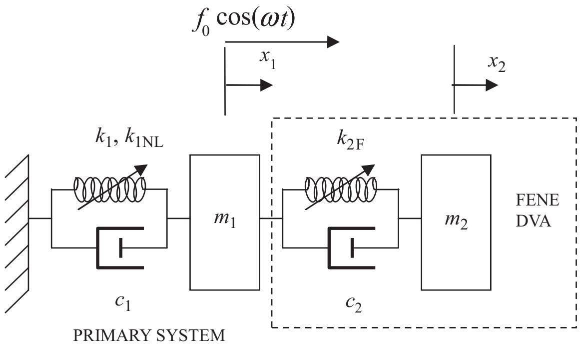

Fig. 1. Schematic representation of a FENE absorber attached to a nonlinear primary system.

$$m_2\ddot{x}_2+c_2(\dot{x}_2-\dot{x}_1)+k_{2F}\frac{(x_2-x_1)}{1-\left(\dfrac{x_2-x_1}{x_0}\right)^2}=0 \tag{4}$$

where m_2 is the mass of the FENE absorber, k_1, k_{NL} and c_1 are the linear and nonlinear stiffness and damping constant of the primary system, respectively, and k_{2F} and c_2 are the coupling stiffness and damping constant for the FENE absorber. Next, we define a normalized time $\tau=\omega t$ and the following parameters are introduced

$$x_r=\frac{x_2-x_1}{x_0},\quad x_s=\frac{x_1}{x_0},\quad \mu=\frac{m_2}{m_1},\quad \omega_{10}=\sqrt{\frac{k_1}{m_1}}$$

$$\overline{\omega}_{10}=\frac{\omega_{10}}{\omega},\quad \epsilon_1=\frac{k_{1NL}}{k_1}x_0^2,\quad \omega_{0F}=\sqrt{\frac{k_{2F}}{m_2}},\quad \overline{\omega}_{0F}=\frac{\omega_{0F}}{\omega}$$

$$\lambda_i=\frac{c_i}{m_i},\quad \overline{\lambda}_i=\frac{\lambda_i}{\omega}\ \ (i=1,2)$$

$$f_0=\frac{f}{x_0m_1},\quad \overline{f_0}=\frac{f_0}{\omega^2} \tag{5}$$

After these replacements, Eqs. (3) and (4) can be written in the following nondimensional form:

$$x_s''+\overline{\lambda}_1x_s'+\overline{\omega}_{10}^2x_s+\epsilon_1\overline{\omega}_{10}^2x_s^3-\mu\overline{\lambda}_2\dot{x}_r-\mu\overline{\omega}_{0F}^2\frac{x_r}{1-x_r^2}=\overline{f}_0\cos(\tau) \tag{6}$$

$$x_r''+\overline{\lambda}_2x_r'+\overline{\omega}_{0F}^2\frac{x_r}{1-x_r^2}=-x_s'' \tag{7}$$

where the prime represents differentiation with respect to τ. The above two formulas can be written in matrix form as

$$\mathbf{M}\mathbf{x}''+\mathbf{C}\mathbf{x}'+\mathbf{K}\mathbf{x}=\mathbf{f} \tag{8}$$

where

$$\mathbf{M}=\begin{bmatrix}1 & 0\\ 1 & 1\end{bmatrix},\quad \mathbf{C}=\begin{bmatrix}\overline{\lambda}_1 & -\mu\overline{\lambda}_2\\ 0 & \overline{\lambda}_2\end{bmatrix},\quad \mathbf{K}=\begin{bmatrix}\overline{\omega}_{10}^2 & \mu\overline{\omega}_{0F}^2\\ 0 & -\overline{\omega}_{0F}^2\end{bmatrix}$$

and

$$\mathbf{x}=\begin{bmatrix}x_s\\ x_r\end{bmatrix},\quad \mathbf{f}=\begin{bmatrix}\overline{f}_0\cos(\tau)+\mu\overline{\omega}_{0F}^2x_r\left(1+\frac{1}{1-x_r^2}\right)-\epsilon_1\overline{\omega}_{10}^2x_s^3\\ -\overline{\omega}_{0F}^2x_r\left(1+\frac{1}{1-x_r^2}\right)\end{bmatrix}$$

3. Method of analysis

In this section we present the analytical treatment of the equations of motion by the method of averaging or Krylov–Bogoliubov–Mitropolsky technique [25]. We adopted this method over others, for example the Method of Multiple Scales [26], because it captures the essential features of saturation phenomenon without requiring to go to very high orders in the perturbation analysis (see Section 4).

In the method of averaging, the steady-state response is assumed as

$$\mathbf{x}(\tau)=\mathbf{u}(\tau)\cos(\tau)+\mathbf{v}(\tau)\sin(\tau) \tag{9}$$

where the time dependence of $\mathbf{u}=[u_s(\tau)u_r(\tau)]^T$ and $\mathbf{v}=[v_s(\tau)v_r(\tau)]^T$ is taken to be "slow". Another condition of the method requires the velocity to have a similar functional form to that of the linear case. A transformation of variables so defined is called a Van der Pol transformation [25]. Thus

$$\mathbf{x}'(\tau)=-\mathbf{u}(\tau)\sin(\tau)+\mathbf{v}(\tau)\cos(\tau) \tag{10}$$

Differentiating Eq. (9) and taking into account Eq. (10) we have

$$\mathbf{u}'(\tau)\cos(\tau)+\mathbf{v}'(\tau)\sin(\tau)=0 \tag{11}$$

Using Eqs. (10) and (11) in evaluating $\mathbf{x}''$ and substituting it in Eq. (8) gives

$$(\mathbf{M}\mathbf{v}'-\mathbf{M}\mathbf{u}+\mathbf{C}\mathbf{v}+\mathbf{K}\mathbf{u})\cos(\tau)-(\mathbf{M}\mathbf{u}'+\mathbf{M}\mathbf{v}+\mathbf{C}\mathbf{u}-\mathbf{K}\mathbf{v})\sin(\tau)=\mathbf{f}(\mathbf{u},\mathbf{v},\tau) \tag{12}$$

Then, Eq. (11) is multiplied by $\mathbf{M}\cos(\tau)$ and Eq. (12) is multiplied by $-\sin(\tau)$. The resulting two equations are then added together. To obtain the final expression, we need to integrate from 0 to 2π the last equation by assuming that $\mathbf{u}$ and $\mathbf{v}$ are constants. As a result, we arrive at

$$\mathbf{M}\mathbf{u}'=-\frac{1}{2}(\mathbf{M}-\mathbf{K})\mathbf{v}'-\frac{1}{2}\mathbf{C}\mathbf{u}-\frac{1}{2}\begin{pmatrix}\mu\overline{\omega}_{0F}^2 v_r\left(1+\frac{2}{\sqrt{1-a_r^2}+1-a_r^2}\right)-\epsilon_1\overline{\omega}_{10}^2\frac{3}{4}v_s a_s^2\\ -\overline{\omega}_{0F}^2 v_r\left(1+\frac{2}{\sqrt{1-a_r^2}+1-a_r^2}\right)\end{pmatrix} \tag{13}$$

In the same way, Eq. (11) is multiplied by $\mathbf{M}\sin(\tau)$, Eq. (12) is multiplied by $\cos(\tau)$ and the two equations are added together. After integration from 0 to 2π of the resulting equation we obtain

$$\mathbf{M}\mathbf{v}'=\frac{1}{2}(\mathbf{M}-\mathbf{K})\mathbf{u}'-\frac{1}{2}\mathbf{C}\mathbf{v}+\frac{1}{2}\begin{pmatrix}\overline{f}_0+\mu\overline{\omega}_{0F}^2 u_r\left(1+\frac{2}{\sqrt{1-a_r^2}+1-a_r^2}\right)-\epsilon_1\overline{\omega}_{10}^2\frac{3}{4}u_s a_s^2\\ -\overline{\omega}_{0F}^2 u_r\left(1+\frac{2}{\sqrt{1-a_r^2}+1-a_r^2}\right)\end{pmatrix} \tag{14}$$

where we have made use of the following definitions: $x_s=a_s\cos(\tau-\phi_s)$, with $u_s=a_s\cos(\phi_s)$ and $v_s=a_s\sin(\phi_s)$; $a_s^2=u_s^2+v_s^2$, and $x_r=a_r\cos(\tau-\phi_r)$, with $u_r=a_r\cos(\phi_r)$ and $v_r=a_r\sin(\phi_r)$; $a_r^2=u_r^2+v_r^2$. The details of the calculation are presented in Appendix Appendix A.

In order to obtain the steady-state solution of Eqs. (13) and (14), one has to set the left-hand side of both equations equal to zero. Then, after a lengthy but straightforward manipulation, we arrive at the amplitude–frequency relation:

$$\begin{aligned}f_0^2-a_r^2\Bigg\{&\left[\left((\omega_{10}^2-\omega^2)+\frac{3}{4}\epsilon_1\omega_{10}^2\left(\frac{\lambda_2^2}{\omega^2}+(A(a_r)-1)^2\right)a_r^2\right)(1-A(a_r))+\lambda_1\lambda_2+\mu\omega^2A(a_r)\right]^2\\&+\left[-\mu\lambda_2\omega-\lambda_1\omega(1-A(a_r))+\frac{\lambda_2}{\omega}\left((\omega_{10}^2-\omega^2)+\frac{3}{4}\epsilon_1\omega_{10}^2\left(\frac{\lambda_2^2}{\omega^2}+(A(a_r)-1)^2\right)a_r^2\right)\right]^2\Bigg\}=0\end{aligned} \tag{15}$$

where $A(a_r)=(\omega_{0F}^2/\omega^2)2/\sqrt{1-a_r^2}+1-a_r^2$. Once the amplitude of the displacement of the relative coordinate has been obtained (a_r), the steady-state solutions for the primary system can be calculated from Eqs. (13) and (14). The final result is

$$a_s=a_r\sqrt{(A(a_r)-1)^2+\frac{\lambda_2^2}{\omega^2}} \tag{16}$$

4. Numerical comparisons and discussion

In this section we present the FRCs corresponding to the steady-state solutions of the system under study. The selected values for the parameters used in Figs. 2, 4 and 6 are presented in Table 1.

The steady-state solutions are determined by setting $\mathbf{u}'=\mathbf{v}'=0$ on the right-hand side of Eqs. (13) and (14) and solving the nonlinear system. The stability analysis is then performed by judging the eigenvalues of the Jacobian matrix of the linearized system calculated at the fixed points.

The aim of this section is to present the dynamic behavior of the proposed system under a variation of some of its parameters and at the same time to study the efficiency of the FENE absorber as the nonlinearity of the primary system increases. Additionally, we compare the performances of the present absorber with the most studied cubic absorber. Finally, direct integration of the equations of motion is performed to verify the accuracy of the proposed solutions.

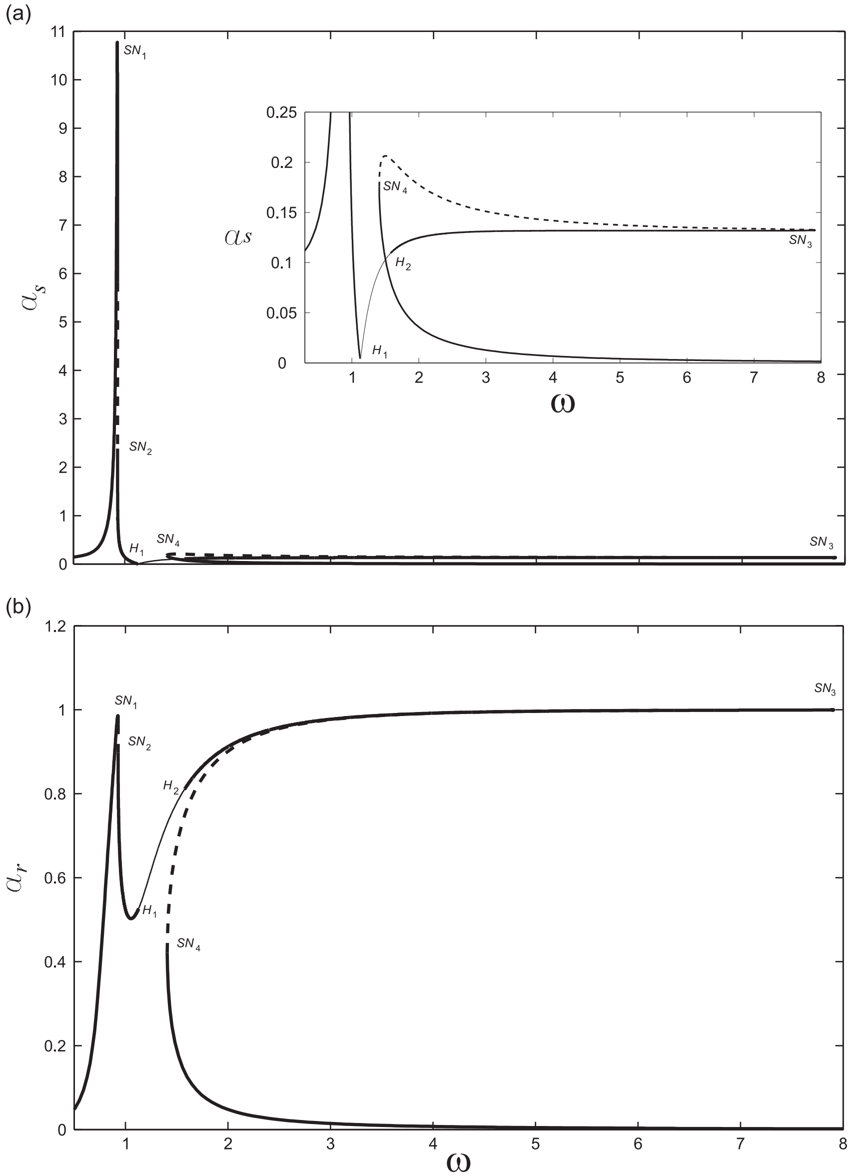

Fig. 2. Frequency–response curves of (a) a_s (amplitude of the displacement of the primary system) and (b) a_r (amplitude of the displacement of the relative coordinate) when $\epsilon_1 = 0$. Solid (dashed) lines denote stable (unstable) equilibrium solutions and thin solid lines denote unstable foci.

Table 1
System parameters for the FRCs of Figs. 2, 4 and 6.

Parameter	λ_1 (s^{-1}) $\left(\xi_1 = \frac{\lambda_1}{2\omega_{10}}\right)$	λ_2 (s^{-1}) $\left(\xi_2 = \frac{\lambda_2}{2\omega_{0F}}\right)$	ω_{10} (s^{-1})	ω_{0F} (s^{-1})	μ	f_0 (s^{-2})	m_1 (kg)	ω_{n1} (s^{-1})	ω_{n2} (s^{-1})
Value	0.01 (0.005)	0.01 (0.005)	1	1	0.15	0.1	1	0.8249	1.2122

4.1. Nonlinearity of the primary system

Here, we study the variation of nonlinearity of the primary system, ϵ_1, to evaluate the performance of the FENE absorber on attenuating the vibration amplitude of the primary system. This is analyzed with the help of the FRCs shown in Figs. 2, 4 and 6 considering a nonlinear cubic parameter $\epsilon_1 = 0$,8, and 35, respectively. The amplitudes $a_{s,r}$ are obtained as functions of the frequency of excitation ω.

The FRCs exhibit an interesting behavior due to saddle-node bifurcations (SN where one of the corresponding eigenvalues crosses the imaginary axis along the real axis from the left to the right-half plane) and Hopf bifurcations

(H where one pair of complex conjugate eigenvalues crosses the imaginary axis transversely from the left to the right-half plane). As a distinctive feature of all the curves, the amplitude of the indirectly excited relative coordinate a_r never exceeds its saturation value of 1, which is indicative of the dynamic behavior of proposed absorber.

When analyzing the case of a linear primary system ($\epsilon_1 = 0$) in Fig. 2(a) and (b), we find that for $0 < \omega < 1.129$ the response of the primary system is identical to that corresponding to a one degree-of-freedom linear system, and that it is not much affected by the presence of the nonlinear absorber – in the sense that it is not bent by the nonlinearity – except from the fact that the solution loses stability via a saddle-node bifurcation when $\omega = 0.9292$ (SN_1). There the response jumps down to another branch of the stable equilibrium solution, which is an example of the nonlinear "jump" effect. From that point on, the nonlinear absorber strongly affects the amplitude and stability of the compound system with respect to the response of a linear compound system, strongly attenuating the response of the higher resonance. As we increase the excitation frequency up to $\omega = 1.129$, the amplitude decreases until the stable equilibrium solution loses stability via a supercritical Hopf bifurcation at H_1 ($\omega = 1.129$). This type of instability has been reported and analyzed in previous works for a cubic nonlinear absorber [13,12], and it was shown to be characterized by a growth of the "linear" free oscillations of the two-degree-of-freedom system of frequencies ω_{n1} and ω_{n2}. In that case, the Hopf bifurcation was the result of a combination resonance of the type $\omega \approx \frac{1}{2}(\omega_{n1} + \omega_{n2})$. As for the FENE absorber, it is apparent that it also exhibits this type of combination resonance due to the odd-parity characteristic of the nonlinear force exerted by the FENE absorber on the primary system. In this regime, the steady-state oscillations are quasi-periodic motions involving possibly much larger amplitudes of vibration than the unstable periodic solutions and they could, in extreme cases, lead to chaos. From the viewpoint of the performance of the absorber in attenuating the response of the primary system, this result is unfavorable.

Fig. 3(a) and (c) shows the variation of the steady-state amplitude of the primary system and the absorber which undergo quasi-periodic motions for two different excitation frequencies in the range $H_1 : H_2$. In Fig. 3(a) an excitation frequency of $\omega = 1.213$ is used, and we can observe that the amplitude of a_s presents an amplification factor of almost four times the value of the corresponding unstable steady-state solution, at the same forcing frequency. Similarly, a_r is also larger than the unstable steady-state solution, but the effect is not so marked. Regarding the character of the limit cycle, Fig. 3(b) shows a period-2 limit cycle involved for these parameters. On the other hand, a better situation from the viewpoint of the performance of the absorber is observed in Fig. 3(c) for $\omega = 1.497$. There, the amplitudes of the quasi-periodic solutions for a_s are only 60% larger than those of the unstable steady-state solution, and the increase for a_r is only about 15%. The limit cycle has also reduced its period to one-half compared to the value in Fig. 3(b) (see Fig. 3(d)).

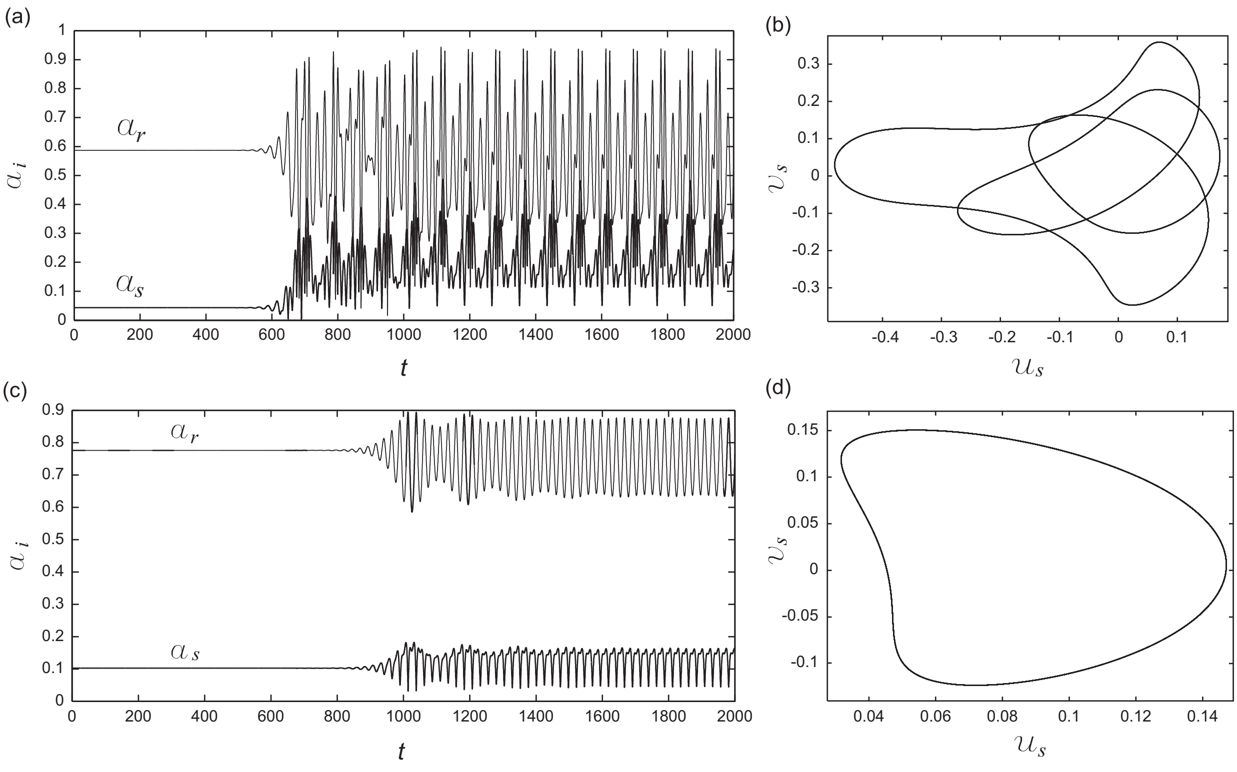

Fig. 3. Quasi-periodic solutions for frequencies in the region $H_1 : 1.129 < \omega < 1.579 : H_2$ of Fig. 2. (a) Time history of a_s and a_r at (a) $\omega = 1.213$, (c) $\omega = 1.497$ and their corresponding two-dimensional projections onto u_s–v_s plane of the phase portrait in (b) and (d), respectively.

Following with the analysis of Fig. 2(a) and (b), once the solution regains its stability via a reverse Hopf bifurcation at H_2 ($\omega = 1.579$), the stable solution grows again in amplitude until arriving to a saddle-node bifurcation SN_3 ($\omega = 7.902$), resulting in the response jumping to another solution branch. On the other hand, above the stable branch which ends into SN_3 it appears an unstable solution branch which starts at the saddle-node bifurcation point SN_4 ($\omega = 1.408$) and ends into SN_3 for increasing frequencies. The stable branch, which also starts in SN_4, regains stability by decreasing its amplitude as the frequency increases, behaving like a linear system.

The FRC of the system considering a nonlinear cubic parameter $\epsilon_1 = 8$ is presented in Fig. 4(a) and (b).

Compared with the previous case (Fig. 2(a)), the amplitude of the main resonance peak of the primary system is five times smaller, evidencing a good performance of the absorber when the nonlinearity of the primary system increases. This fact is observed in the peak bending towards the higher frequencies (hardening-spring type response), which makes not only the peak smaller but also the whole FRC for the region of the primary resonance. The unstable solution limited by the Hopf bifurcations exists between $H_1 : 1.129 < \omega < 1.825 : H_2$. Compared to the case of $\epsilon_1 = 0$, the foci solution increases its range of existence.

Another region of quasi-periodicity limited by Hopf bifurcations exists for $H_3 : 4.154 < \omega < 7.925 : H_4$. It is remarkable that this region does not appear in the case of $\epsilon_1 = 0$, or for a cubic oscillator, and it seems to be characteristic of this type

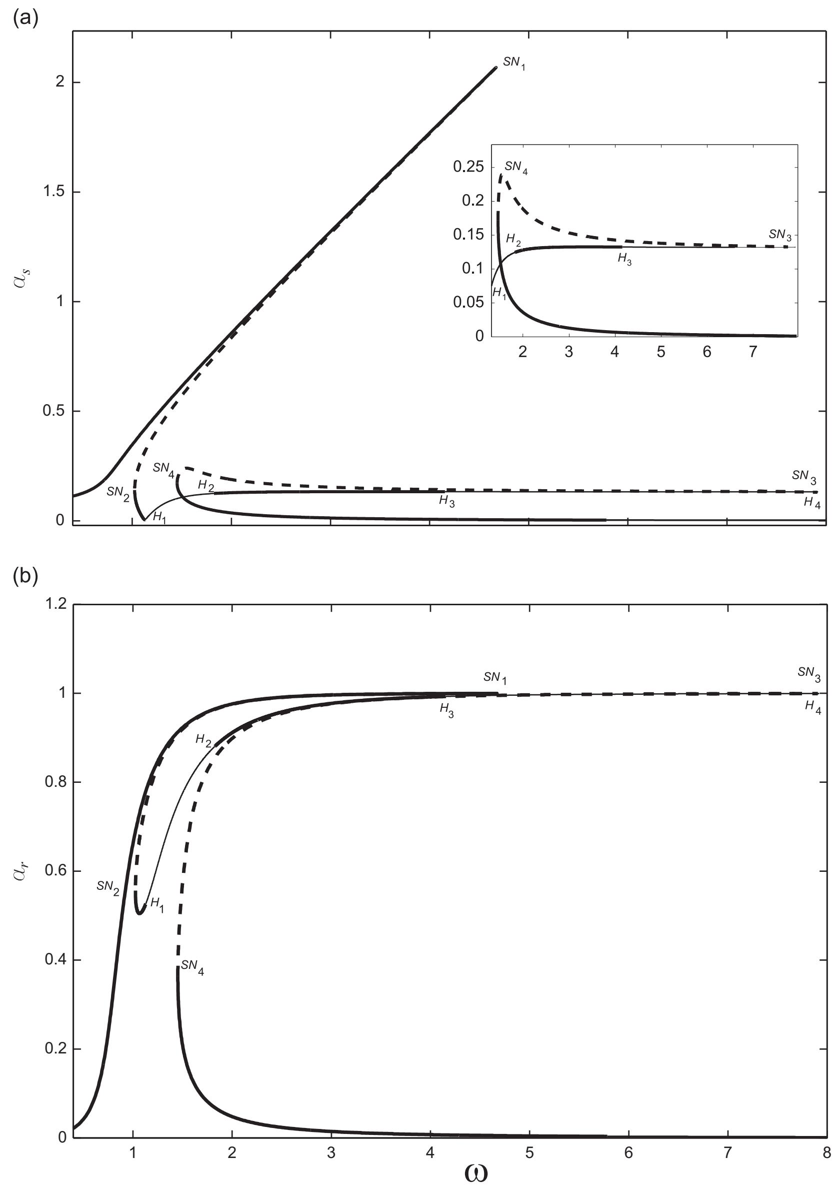

Fig. 4. Frequency–response curves of (a) a_s and (b) a_r when $\epsilon_1 = 8$. Solid (dashed) lines denote stable (unstable) equilibrium solutions and thin solid lines denote unstable foci.

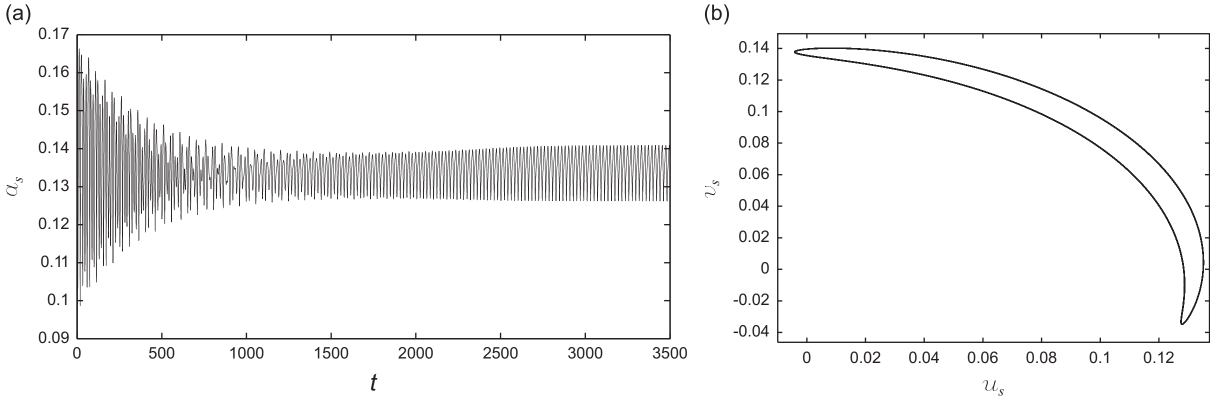

Fig. 5. (a) Time history of a_s at $\omega = 4.362$ when $\epsilon_1 = 8$. (b) Phase portrait of the components u_s and v_s at the same frequency.

of nonlinear absorber. In order to see the behavior of the system in this region, we plot in Fig. 5(a) the time history of a_s for an excitation frequency of $\omega = 4.362$. As initial condition, the system is released from a point between the branches $H_3 : H_4$ and $SN_4 : SN_3$. Clearly the amplitude of the limit cycle, which starts to develop after a time of approximately 1000 s, is limited by the unstable branch of solution ($SN_4 : SN_3$) and it does not grow much compared to the unstable steady-state solution. Therefore, the absorber shows an acceptable behavior and there is no risk of an amplification of the vibration levels as in the case of quasi-periodic oscillations in the region $H_1 : H_2$. An interesting question that may be asked is how the behavior of the steady-state solution is for larger ω's. Although not shown here, we have carried out a study of the quasi-periodic solutions that start in H_3 using a numerical continuation of the limit cycle and we have found that the limit cycle is still present until $\omega = 4.369$. There, it intersects the unstable steady-state solution and, after developing a transient behavior, it finally evolves to the stable steady-state solution of low amplitude observed in Fig. 4(a).

For the limit case of strong nonlinearity of the primary system, $\epsilon_1 = 35$, the FRCs are shown in Fig. 6(a) and (b). It can be observed that the behavior of the system becomes more and more complex. Multiple saddle-node and Hopf bifurcations appear and disappear in the region under study ($0 < \omega < 8$). A very interesting feature in this case is seen for a_r. In the process of this parameter change (ϵ_1), the appearance of an almost detached curve that lies inside the resonance curve indicates the existence of another response branch of the primary system. This is in fact confirmed in Fig. 6(b), where the emerging solution branch is enclosed by the labels $SN_9 - SN_{10}$ and $H_7 - H_8$. Although the existence of a similar behavior for nonlinear cubic absorbers has been previously reported [5,27] in those cases the bubble could lie outside the main resonance response, resulting in larger steady-steady responses of the stable solutions. However, this is not possible in our case due to the saturation phenomenon of the absorber. Hence, the presence of an almost detached curve that lies only inside the FRC seems to be a distinctive feature of this type of absorbers. Focusing on the analysis of the response, we observe that it presents multi-valued solutions for the range $1.574 < \omega < 3.871$, where multiple saddle-node and Hopf bifurcations appear simultaneously. The stable equilibrium solution loses and regains its stability in a nontrivial form which is due to the strong nonlinearity of the system. There are four foci solution branches limited by Hopf bifurcations, namely Branch I $H_1 : 1.129 < \omega < 1.403 : H_2$, Branch II $H_3 : 1.474 < \omega < 1.724 < H_4$, Branch III $H_5 : 1.626 < \omega < 7.94 : H_6$ and Branch IV $H_7 : 2.254 < \omega < 3.868 : H_8$; and multiple saddle-node points namely, $SN_1 - SN_2$, $SN_3 - SN_4$, $SN_5 - SN_6$, $SN_7 - SN_8$ and $SN_9 - SN_{10}$. Despite the complexity of the system in this region, it is important to highlight that the peak magnitude of the main stable resonance branch strongly decreases compared to the case in Fig. 4(a) (almost 25%). The disadvantage of this complex behavior is, naturally, the multiple regions of instability emerging from Hopf bifurcations with quasi-periodic and possible chaotic motions.

4.2. Parameters of the absorber

In this section we analyze the effect of damping (λ_2), the variation of the linearized frequency (ω_{0F}) and the variation of the mass ratio (μ) on the dynamic behavior of the primary system. It is expected that a large value of damping of the absorber, for a given value of its linearized frequency will turn the system more stable at the instability regions due to the saddle-node or Hopf bifurcations. At the same time, changing the ratio $\rho = \omega_{0F}/\omega_{01}$ will also tend to change the stability character of the solutions potentially removing the unfavorable high amplitudes of the quasi-periodic motions according to previous studies on cubic absorbers [13,28]. Lastly, modifying the mass ratio (μ) may affect the effectiveness of the FENE absorber. For the following analysis, we selected as fixed parameters those corresponding to the primary system, namely: $\epsilon_1 = 8$, $\omega_{10} = 1$; $\mu = 0.15$; $\lambda_1 = 0.01$, $m_1 = 1$ and $f_0 = 0.1$. And for the absorber we also select $\lambda_2 = 0.01$, $\omega_{0F} = 1$ unless some of them are deliberately changed for the proposed studies.

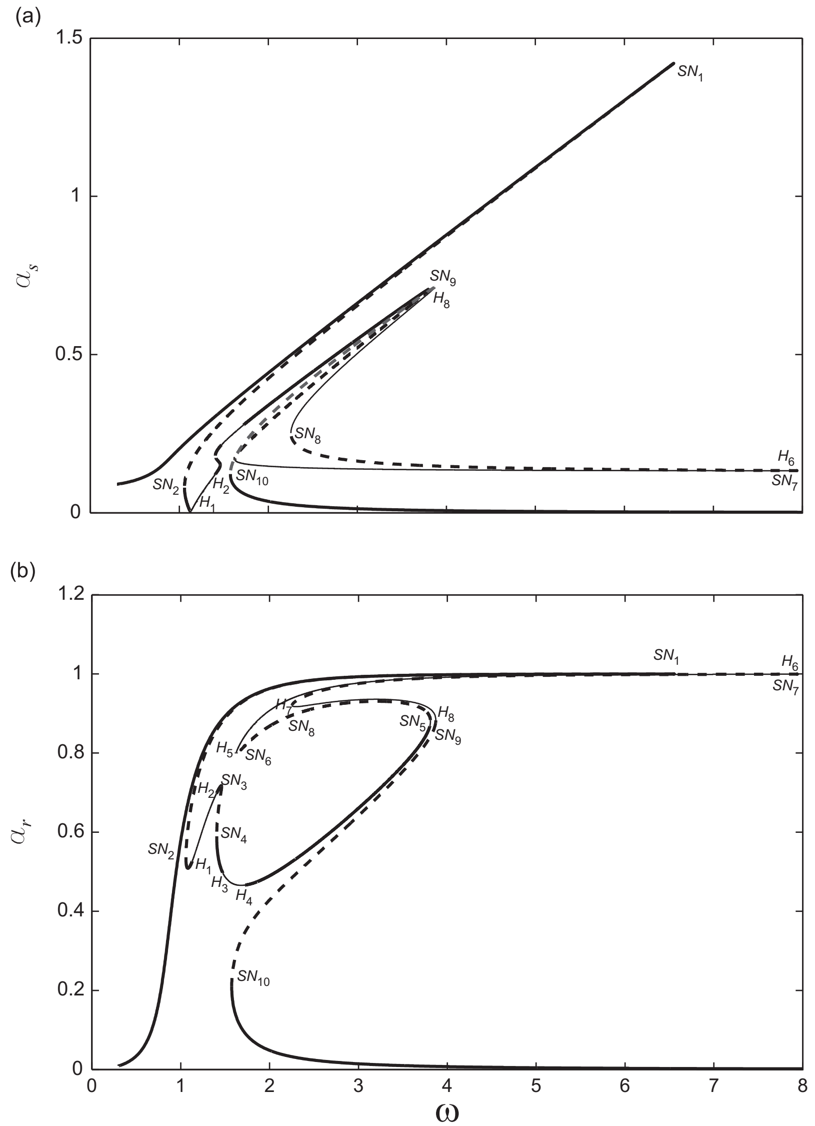

Fig. 6. Frequency–response curves of (a) a_s and (b) a_r when $\epsilon_1 = 35$. Solid (dashed) lines denote stable (unstable) equilibrium solutions and thin solid lines denote unstable foci.

4.2.1. Damping

The effect of the damping of the absorber on the FRCs is examined in Figs. 7 and 8. The FRC presented in Fig. 4(a) and (b) are compared with Fig. 7(a), (b) when λ_2 is increased from $\lambda_2 = 0.01 \rightarrow 0.05$. The first observed distinctive feature is the increasing size of the instability region generated through Hopf bifurcations labelled by $H_1 : H_2$. This suggests that increasing the damping ratio up to this value does not turn the system more stable and, conversely, enlarges the region of quasi-periodic motions. Another characteristic aspect of the same figure is that the region $H_3 : H_4$ has disappeared and only the branch limited by $SN_4 : SN_3$ still exists. Regarding the maximum value of a_s, which is important for the performance of the absorber, a decrease in the magnitude of the main resonance peak (labelled SN_1) can be observed, compared to the same point in Fig. 4(a) from $a_s \approx 2.07$ to $a_s \approx 1.64$. This represents a reduction of more than 20%. Finally, Fig. 7(b) presents the FRC for a_r. Analyzing only the differences between this figure and Fig. 4(b), it can be noticed that the second resonance branch has decreased, having a maximum value of $\omega \approx 2.5$ instead of $\omega \approx 8$ (SN_3). Naturally, all branches in this case remain bounded, due to the finite extension of the relative coordinate.

A larger value of $\lambda_2 = 0.3$ is considered in Fig. 8(a) and (b). In this case, the second resonant branch straightens up in an attempt to regain stability. As a result, the instability region $H_1 : H_2$ has decreased considerably, suggesting that an increment of λ_2 from $0.05 \rightarrow 0.3$ makes the system more stable in this region. An expected limit case of this situation is plotted in Fig. 8(c) and (d) where the FRCs for $\lambda_2 = 0.4$ shows the absence of the region $H_1 : H_2$.

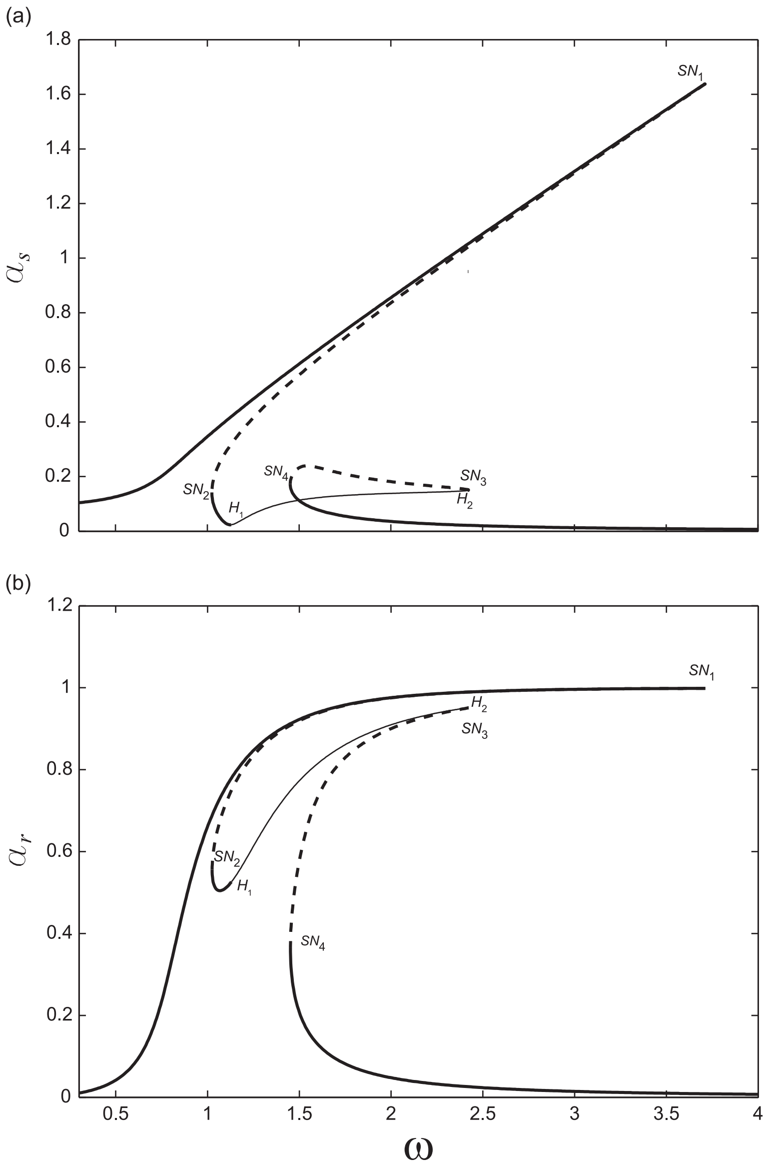

Fig. 7. Frequency–response curves of (a) a_s and (b) a_r when $\epsilon_1 = 8$ and $\lambda_2 = 0.05$.

Using the same parameters as in Fig. 8(a) and (b), the limit cycle, which begins in H_1 and ends in H_2, is presented in Fig. 9. It is interesting to observe that the generated limit cycle (solid circles) is stable and the value of a_s is not excessively large (with a maximum of $a_s = 0.3$ for $\omega \approx 1.32$). This demonstrates, in a very illustrative way, that the developed instability which causes quasi-periodic oscillations does not always give rise to uncontrollable large amplitudes for the primary system. In this sense, the absorber shows a good performance for this set of parameters.

4.2.2. Linearized frequency

In the following section, we analyze the effect of the variation of the linearized frequency of the absorber on the FRCs and how this variation possibly affects the stability of the observed steady-state solutions. To this end, we quote a well-known fact from the theory of nonlinear absorbers: if one introduces internal resonances in the system, for example $\omega_{n2} \approx 3\omega_{n1}$ the unfavorable high amplitudes of the quasi-periodic motions can be reduced for the region of a combination resonance [28]. The physical reason for this is that the amplitudes of the steady-state quasi-periodic motions can be mitigated by an energy-sharing between the modes of the linearized system.

In order to explore this result for our nonlinear absorber, the first analysis is performed for $\omega_{0F} = 2.55$. The other parameter values are the same as those used in Fig. 4(a) and (b). For these parameter values, the linearized natural frequencies of the system are $\omega_{n1} = 0.9235$, $\omega_{n2} = 2.7614$, giving $\omega_{n2} \approx 3\omega_{n1}$. The corresponding FRCs are shown in

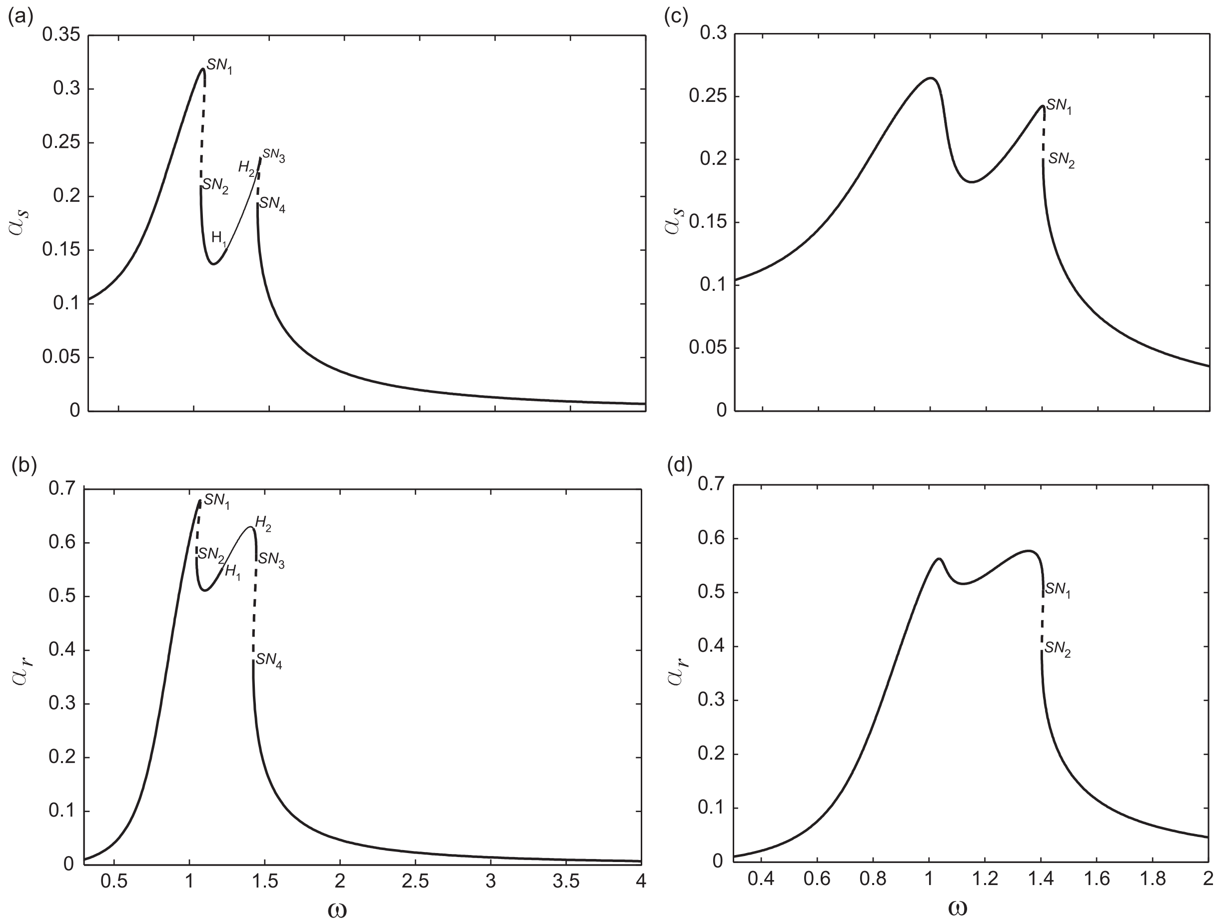

Fig. 8. Different FRCs of (a) a_s and (b) a_r when $\lambda_2 = 0.3$ and (c) a_s and (d) a_r when $\lambda_2 = 0.4$.

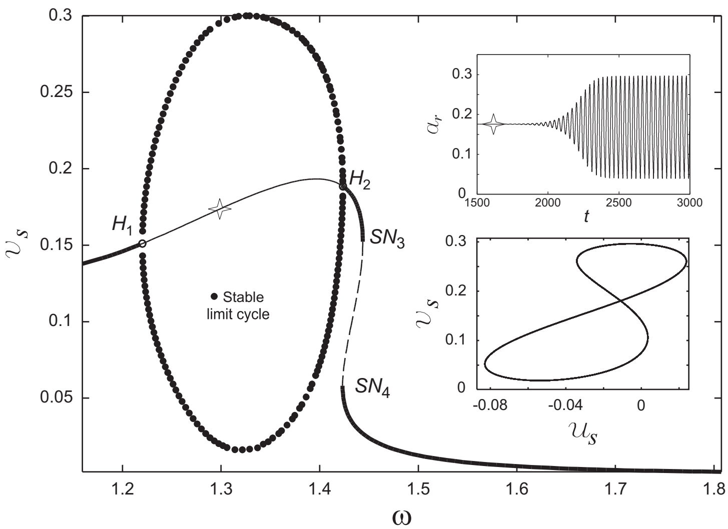

Fig. 9. Visualization of the limit cycle between the Hopf bifurcations H_1 and H_2 for the system of Fig. 8. In the inset, the time history of a_s and the two-dimensional projections onto the $u_s - v_s$ plane of the phase portraits of the limit cycle found at $\omega = 1.3$ are presented.

Fig. 10(a) and (b). There, it can be observed that the region of quasi-periodic solutions has disappeared and a region of low amplitude stable solutions has emerged instead. A possible physical explanation appears to be related to the shift of the frequency of maximum absorption to larger frequencies due to the detuning between ω_{n1} and ω_{n2}. It is also important to

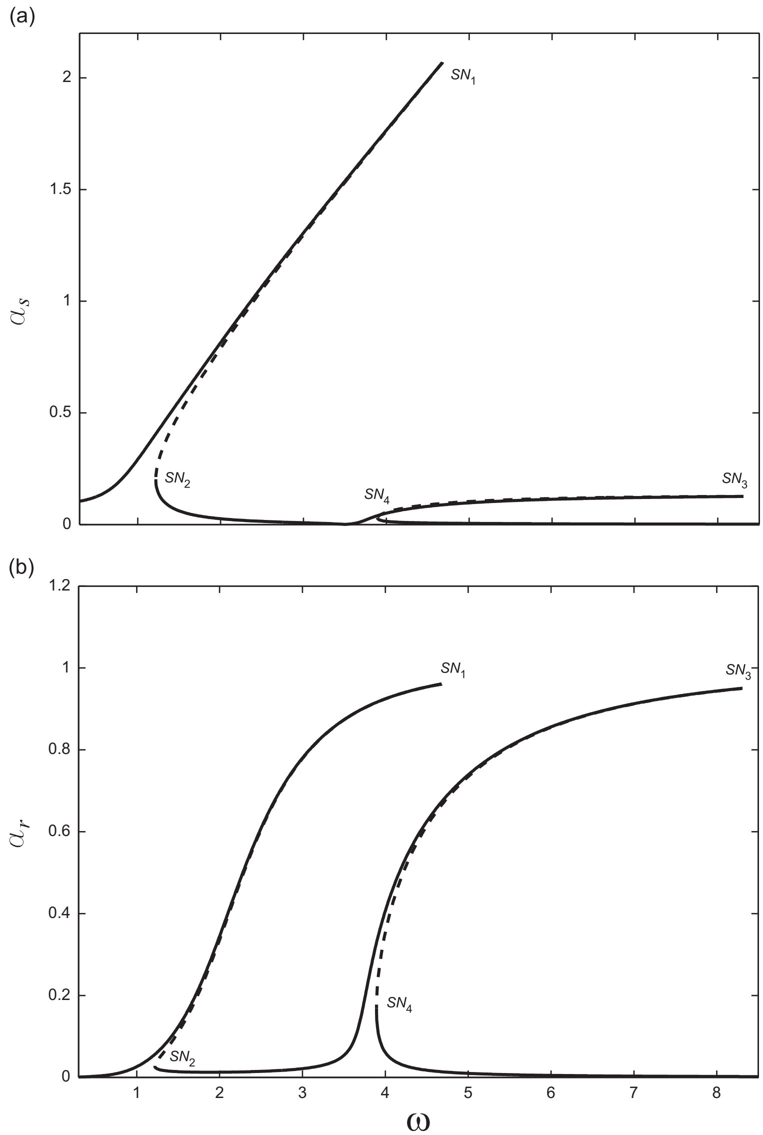

Fig. 10. Frequency–response curves of (a) a_s and (b) a_r when $\epsilon_1=8$ and $\omega_{n2}\approx 3\omega_{n1}$ (internal resonance case).

point out that the peak magnitude of the main resonance does not suffer any change with respect to its counterpart in Fig. 4(a), which shows certain robustness of the absorber under this change.

For our second analysis we consider $\omega_{0F}=2$. In this case, the system is not under an internal resonance condition: $\omega_{n2}=2.3798\omega_{n1}$. The purpose of this analysis is to see whether the system is still able to maintain the stability in the region of possible combination resonance $2\omega\approx\omega_{n1}+\omega_{n2}=1.549$. The resulting FRCs are shown in Fig. 11(a) and (b). When we compare Fig. 11(a) with Fig. 4(a) it is clear that the region of quasi-periodic solutions $H_1:H_2$ has again disappeared, presenting a stable steady-state solution instead.

Summarizing, it can be concluded that the absence of quasi-periodic solutions for the selected set of parameters (which is favorable from a vibration control viewpoint) can be achieved by a detuning between the primary system and the absorber, not only for an internal resonance condition, but also in the case when the ratio between the linear frequency of the absorber and the primary system is at least more than two.

4.2.3. Mass ratio

The effect of a variation of the mass ratio on the FRC of the primary system is shown in Fig. 12. We consider three different values of $\mu=0.05$ (black), 0.1 (red) and 0.2 (green). In order to vary only one parameter at a time, we set $\rho=\omega_{0F}/\omega_{01}=1$ for all cases. The dynamical response is qualitatively similar in the three cases; however, an increase in

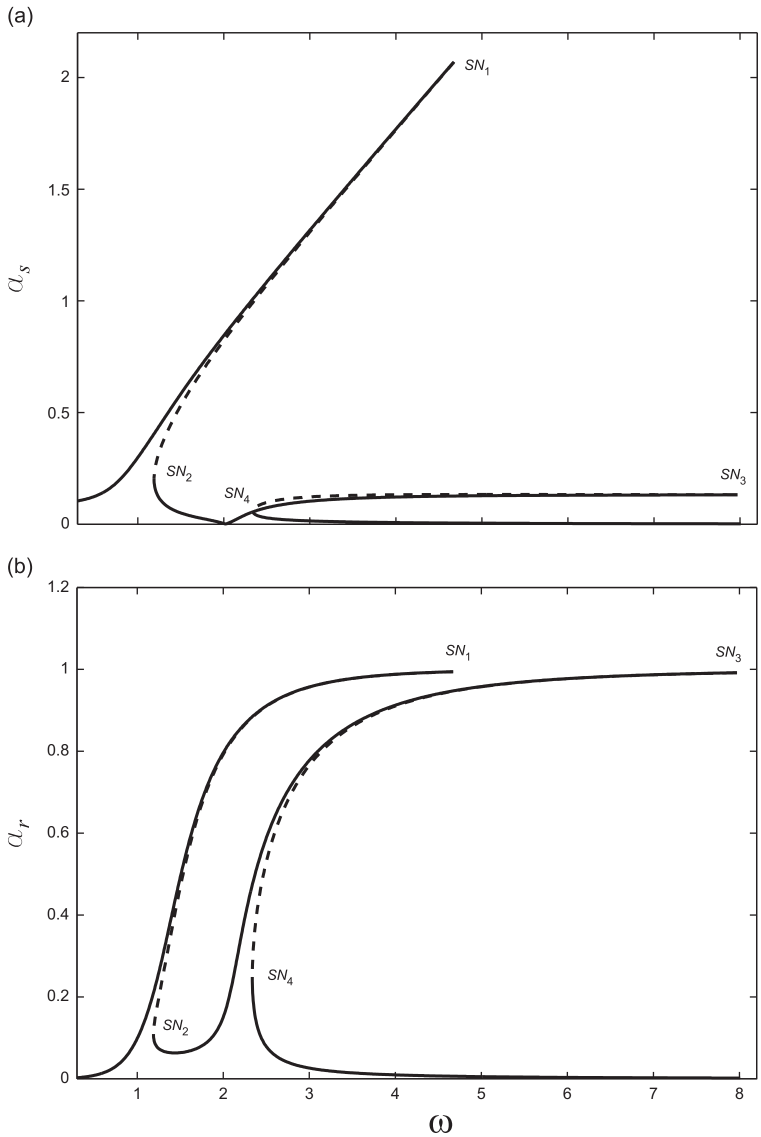

Fig. 11. Frequency–response curves of (a) a_s and (b) a_r when $\epsilon_1 = 8$ and $\omega_{n2} = 2.3798\ \omega_{n1}$ (non-commensurable frequencies)

the unstable foci solution can be observed as the mass ratio increases. For example, the largest size of the unstable foci solution bounded by the two Hopf bifurcations H_1 and H_2, corresponds to $\mu = 0.2$ (green curve). Therefore the solution loses and regains stability for a smaller and larger forcing frequency of approximately $\omega = 1.11$ and $\omega = 1.87$, respectively. Also in the latter case, the stable periodic amplitudes are always larger in comparison with the other cases. As a conclusion, it can be said that a larger mass ratio does not imply a better mitigation of the amplitude of vibration of the primary system or a smaller region of quasi-periodic motions for the cases studied.

4.3. Comparison with a cubic absorber

In this section, the FRCs obtained for an absorber with cubic nonlinearity is evaluated in order to conduct a comparison with the proposed FENE absorber. The mathematical model of the cubic absorber is presented in the following equations:

$$x_s'' + \overline{\lambda}_1 x_s' + \overline{\varpi}_{10}^2 x_s + \epsilon_1 \overline{\varpi}_{10}^2 x_s^3 - \mu \overline{\lambda}_2 \dot{x}_r - \mu \overline{\varpi}_{0F}^2 x_r - \overline{\alpha} x_r^3 = \overline{f}_0 \cos(\tau) \tag{17}$$

$$x_r'' + \overline{\lambda}_2 x_r' + \overline{\varpi}_{0F}^2 x_r + \frac{\overline{\alpha}}{\mu} x_r^3 = -x_s'' \tag{18}$$

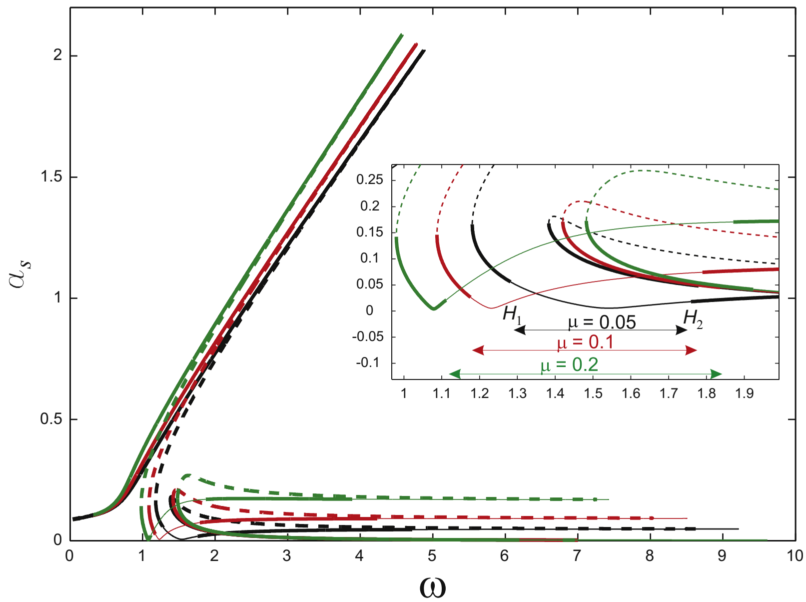

Fig. 12. Frequency–response curves of a_s for three different mass ratios: $\mu = 0.05$ (black), 0.1 (red) and 0.2 (green). (For interpretation of the references to color in this figure caption, the reader is referred to the web version of this article.)

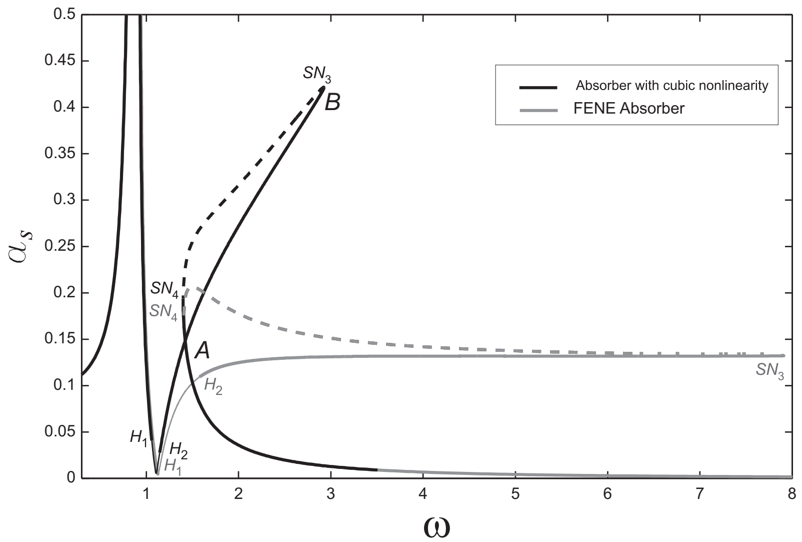

Fig. 13. Comparison between the FRCs of the primary system (a_s) for a FENE absorber and a cubic absorber. Linear primary system ($\epsilon_1 = 0$).

where we define $\overline{\alpha} = \alpha/\omega^2$ and α is the nonlinear parameter for the cubic absorber [26]. In order to perform a meaningful comparison between the cubic and FENE absorber we adopt $\alpha = \mu\omega_{0F}^2$. Eqs. (17) and (18) are solved by means of the method outlined in Section 3.

Figs. 13 and 14 show a comparison between both models, considering a nonlinear cubic parameter of the primary system $\epsilon_1 = 0$ and 8, respectively. The FRC of the primary system for the cubic absorber is shown in black color, and that for the FENE model in gray. It can be observed that the periodic branches, represented by saddle-node and Hopf bifurcations are similar in both models. Furthermore, the unstable foci solution is present in both models for a similar frequency range. For the case of $\epsilon_1 = 0$, in the stable region bounded by A and B the FENE absorber performs a larger attenuation than the cubic absorber, whereas the unstable foci solution is larger for the FENE absorber. When the nonlinearity is increased to $\epsilon_1 = 8$, it can be clearly observed that the FENE response is smaller for the whole considered frequency range in comparison with the cubic absorber. It is remarkable to point out that the first resonance peak is almost two times smaller in the proposed absorber. Taking all these considerations into account, the proposed model exhibits a better performance in comparison with the cubic model for a strong a nonlinearity of the primary system ($\epsilon_1 = 8$).

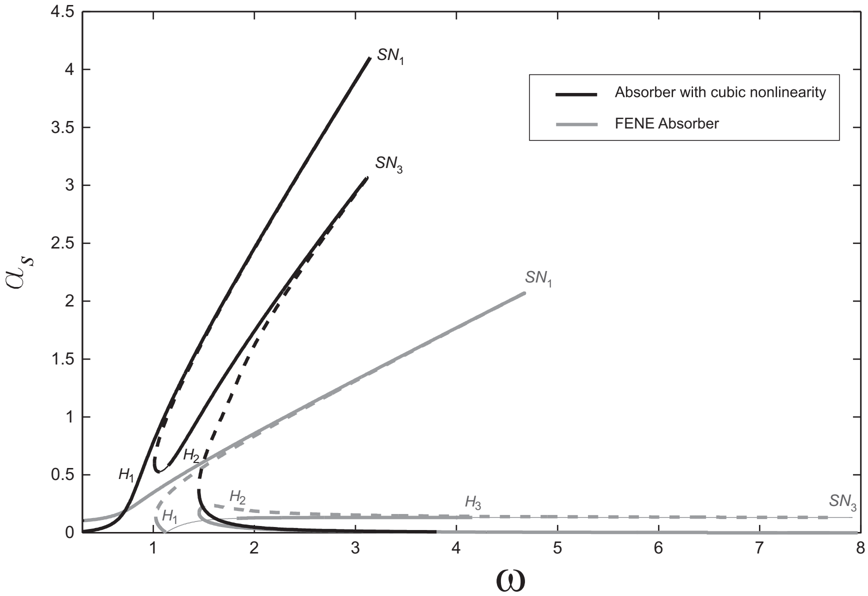

Fig. 14. Comparison between the FRCs of the primary system (a_s) for a FENE absorber and a cubic absorber. Nonlinear primary system with $\epsilon_1 = 8$.

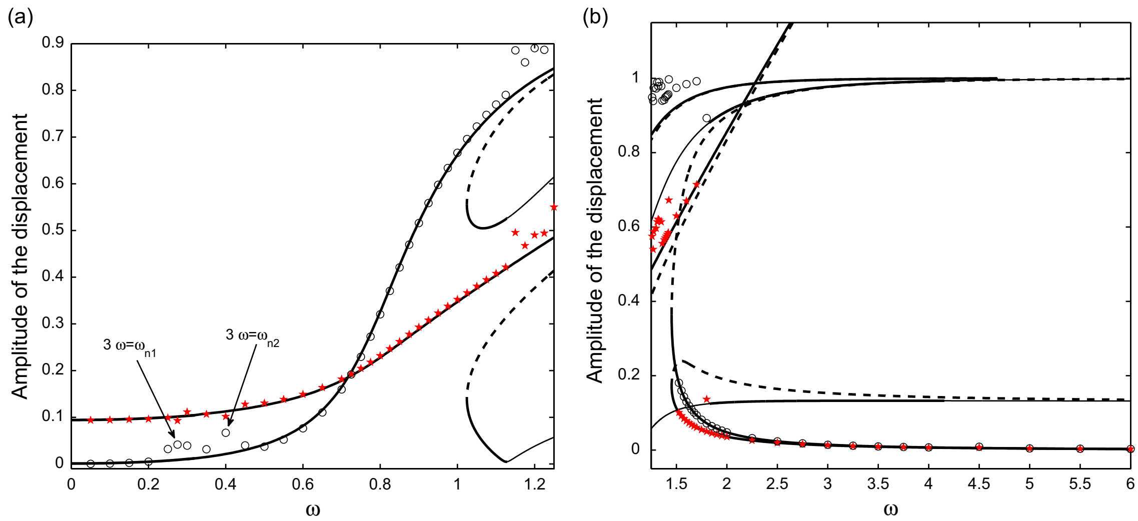

Fig. 15. Comparison between the analytically obtained FRC of Fig. 4 (solid and dashed lines) and that obtained by direct integration of the equations of motion a_s (stars), a_r (circles) (a) for $0 < \omega < 1.25$ where secondary (superharmonic) resonances occur (b) for region $1.25 < \omega < 6$.

4.4. Numerical integration and comparisons

In this subsection we perform a direct numerical integration of the equations of motion equations (6) and (7) to verify the accuracy of the proposed model. The numerical results were obtained by solving the corresponding differential equations and calculating the amplitude of the time series solution of the steady-state response of a_s and a_r. These are shown in Figs. 15(a), (b) and 16. We use the symbol stars for a_s and circles for a_r, and adopt the numerical values of Fig. 4(a) and (b) for all cases. The computation was performed starting with $\omega = 0$ with initial conditions given by $[x_s, \dot{x}_s, x_r, \dot{x}_r] = [0,0,0,0]$, and then the excitation frequency ω was increased gradually at small incremental steps $\delta\omega$ up to $\omega = 6$. For the initial conditions for the next driving frequency we selected the steady-state solution of the previous frequency. We also performed the calculations for decreasing values of ω to explore the hysteresis of the system.

For a better presentation of the results, we show them in three figures corresponding to three frequency regimes. Fig. 15(a) shows the region of low frequencies $0 < \omega < 1.25$ and Fig. 15(b) illustrates the region for high frequencies $1.25 < \omega < 6$. Due to the complexity of the solutions obtained, we plot in Fig. 16 the middle frequency regime $1 < \omega < 1.85$. In the first region (Fig. 15(a)), it is possible to observe a perfect agreement between the numerical and the proposed

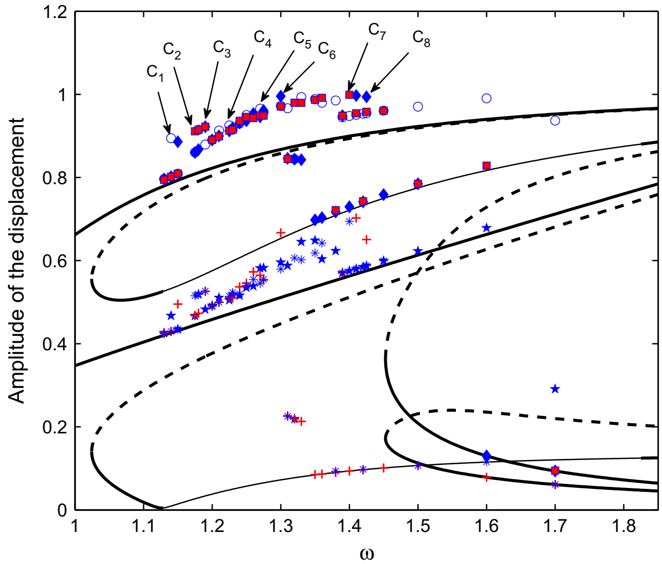

Fig. 16. Comparison between the analytically obtained FRC of Fig. 4 (thick solid, thin solid and dashed lines) and that obtained by direct integration of the equations of motion for the intermediate frequency region $1<\omega<1.75$, considering different initial conditions (see text): previous a_s (stars), a_r (circles), null a_s (+), a_r (diamonds) and intermediate a_s (asterisks), a_r (squares). Points C_1-C_7 refer to different kinds of solutions (see text).

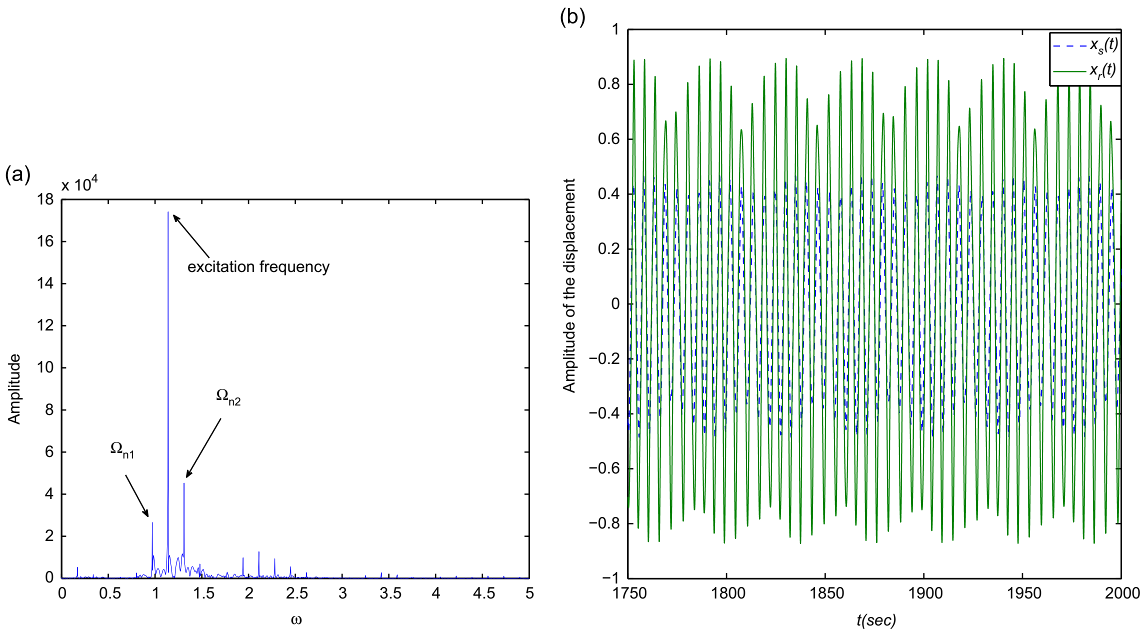

Fig. 17. (a) Fourier spectrum of x_s and (b) time domain response of the steady-state solution of the numerical integration of the equations of motion for $C_1:\omega=1.14$.

solution for both amplitudes a_s and a_r. However, there are two points where both methods differ. These points correspond to the presence of superharmonic resonances, and they were not included in the proposed analytical formulation of the problem. The first one is found at $\omega=0.275$ and implies that $3\omega=\omega_{n1}$ and the second one, which is at $\omega=0.4$, corresponds to $3\omega=\omega_{n2}$. The latter is clearly observed in response a_r while in a_s the resonance conditions are slightly shifted to the right. This is attributed to the amplitude-dependent character of the natural frequencies ω_{n1} and ω_{n2}. For the high frequency regime, Fig. 15(b), the numerical results are in good agreement with those predicted by the proposed model.

Finally, we arrive at the consideration of Fig. 16. Most of the results of the computations show a region of poor agreement between both solutions. The reason for this is that the curves obtained by the proposed method give us the amplitude of the periodic solutions (FRC) whereas the corresponding numerical solution shows the total response of the system which may consist of periodic, quasi-periodic or even chaotic contributions to the response.

Note that for these frequencies three solution branches coexist: one corresponds to a stable steady-state motion (high amplitude) and the other two correspond to unstable motions. Of these last two, the one with lower amplitude is characterized by a region of quasi-periodic oscillations and, in extreme cases, possible chaotic motions. To compute all these attractors, we selected three different initial conditions (a–c) given by the following rules: (a) initial conditions equal to those in Fig. 15(a) and (b) (referred to as previous in Fig. 16); (b) zero initial conditions, referred to as null, and (c) an intermediate initial conditions (intermediate). As a first conclusion it is possible to observe that the amplitudes depend on the selected initial conditions. For example, for the initial condition called (a), the amplitude remains above the higher (stable) solution branch for all the studied frequencies. In contrast, (b) and (c) have amplitudes which fluctuate between the higher (stable) branch and the lower (unstable) branch. To analyze this further, we studied the character of the solution for some selected points labelled C_1-C_8 in Fig. 16. These points correspond to some relative maxima. For the first point $C_1 : \omega = 1.14$, the Fourier spectrum of the steady-state solution of x_s and its time domain response are plotted in Fig. 17(a) and (b), respectively. Fourier spectrum reveals two distinctive features of the solution: the first one is that the steady-state response has a multi-frequency character and the second one is that the major contributions come from two harmonic components of frequencies $\Omega_{n1} \approx 0.98$ and $\Omega_{n2} \approx 1.319$. Since they differ from the linearized frequencies ω_{n1} and ω_{n2} due to the amplitude-dependent character of the natural frequencies of nonlinear systems, we label them with capital letters. The time domain response of the solution is given in Fig. 17(b). There we can observe the amplitude-modulated characteristic oscillation of the displacement amplitude a_r (solid line) and a_s (dashed line) which correspond to quasi-periodic motions. Following with the analysis, we observe that for points $C_2 : \omega = 1.175$, $C_3 : \omega = 1.19, C_4 : \omega = 1.225, C_5 : \omega = 1.27$ and $C_7 : \omega = 1.4$ the solutions are very similar to those shown for C_1: they present two major contributions from harmonic components of frequencies Ω_{n1} and Ω_{n2} (with different values compared to C_1) and the response is quasi-periodic. Nevertheless, the situation for $C_6 : \omega = 1.25$ and $C_8 : \omega = 1.425$ is rather different. Although the contributions to the solution from frequencies Ω_{n1} and Ω_{n2} are still present, an almost continuum contribution from other frequencies appears in the motion, clearly indicating a chaotic behavior for these frequencies. Fig. 18(a–d) shows the Fourier spectra of x_s together with the time domain response for points C_6 (Fig. 18(a–b)) and C_8 (Fig. 18(c–d)). There, the characteristic non-periodic and multi-frequency character of the solution confirms the chaotic motion of the response.

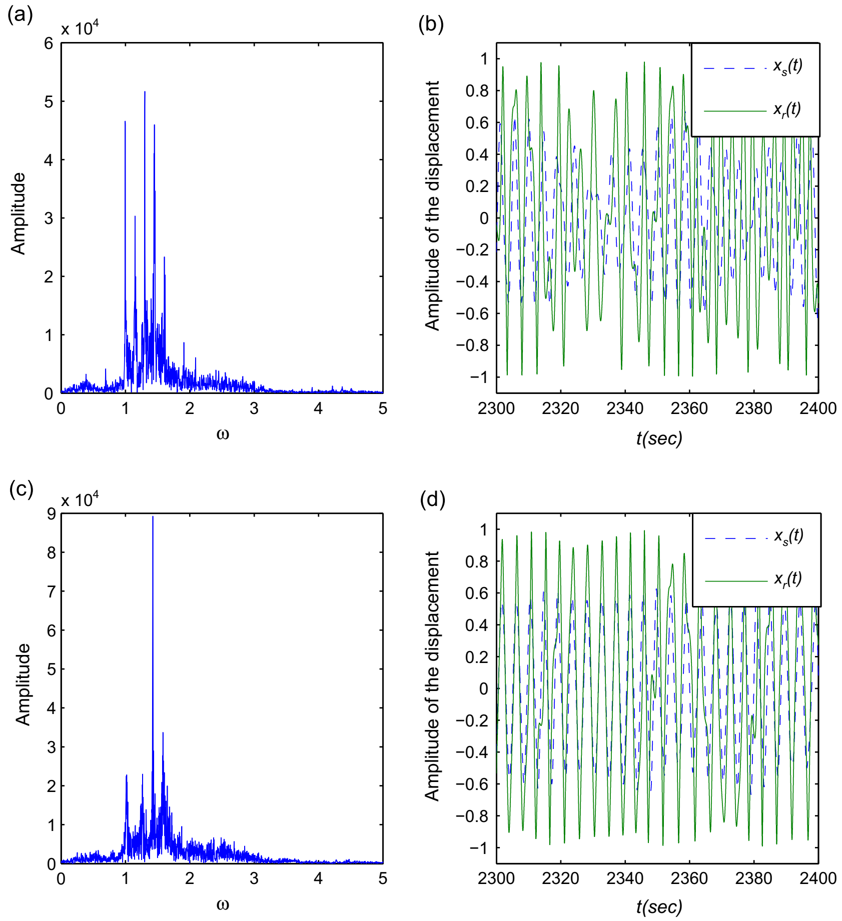

Fig. 18. (a) Fourier spectrum of x_s and (b) time domain response for C_6 (numerical solution), (c) Fourier spectrum (x_s) and (d) time domain response for C_8 (numerical solution).

5. Conclusions

In this work we analyze the dynamics of a novel nonlinear dynamic vibration absorber attached to a linear/nonlinear primary system. The method of averaging was selected to obtain the FRCs, which proved to be appropriate to model the saturation phenomenon of the absorber. A distinctive feature of the dynamic behavior of the system is that the amplitude of the indirectly excited relative coordinate never exceeds a maximum value of one (normalized amplitude). From the studied cases, it is possible to draw the following main conclusions:

- The proposed absorber has a very good efficiency when the nonlinearity of the primary system increases. For example, it was observed that in the case of $\epsilon_1 = 8$, the maximum amplitude recorded for the main resonance peak was five times smaller compared with the linear case ($\epsilon_1 = 0$).
- A comparison with a cubic nonlinear absorber shows that the effectiveness of the FENE absorber exhibits a better performance in comparison with the cubic model for a strong nonlinearity of the primary system ($\epsilon_1 = 8$).
- A possible disadvantage of nonlinear absorbers, and of our proposed absorber too, can be the presence of quasi-periodic oscillations of high amplitudes coexisting with unstable periodic solutions. It was demonstrated for the studied cases that it is possible to eliminate this effect by means of a detuning between the primary system and the absorber, for a low damping of the absorber, or by adding a large amount of damping to the absorber.

Additionally, a parameter study of the proposed system yields the following results:

- When the nonlinearity of the primary system is increased, the number of dynamic instabilities (saddle-node and Hopf bifurcations) increases, but the effectiveness of the absorber increases as well.
- An expected decrease (increase) in the amplitude of the primary system was observed for an increase (decrease) in the amount of damping of the absorber. Regarding the persistence of the region of combination resonance $H_1 : H_2$, different behaviors are observed depending on the amount of damping. For $0.01 < \lambda_2 < 0.05$ the region $H_1 : H_2$ grows. On the other hand, for the value $0.05 < \lambda_2 < 0.3$ the region decreases and it finally disappears for $\lambda_2 = 0.4$.
- A variation of the linear frequency of the absorber (for a lightly damped absorber) reveals the absence of Hopf bifurcations and hence of quasi-periodic motions. This is observed not only for an internal resonance condition, but also for non-commensurate frequencies. In the latter case, this effect is observed for a frequency ratio between the primary system and the absorber larger than two.
- The increase in mass ratio produces an increase in the stable periodic amplitudes of the primary system and a widening of the region of unstable foci.

Finally, as a result of direct comparison of the proposed solution with the direct integration of the equations of motion, it can be concluded that a perfect agreement is observed in those cases, where neither secondary nor combination resonances take place. In these cases an analytic continuation of the emerging limit cycle solutions is needed in order to generate a more approximate solution.

Acknowledgments

M. Febbo wishes to acknowledge the financial support of CONICET, Agencia Nacional de Promocion Científica y Tecnológica under Grant PICT 2008 No. 0423 and Secretaría de Ciencia y Tecnología UNS. S.P. Machado acknowledges CONICET and Secretaría de Ciencia y Tecnología UTN FRBB.

Appendix A. Derivation of some useful integrals

In applying the procedure to obtain Eqs. (13) and (14) we will find integrals of the following type:

$$\int_0^{2\pi} \mu\overline{\omega}_{0F}^2 \frac{x_r}{1-x_r^2} \begin{Bmatrix} \cos(\tau) \\ \sin(\tau) \end{Bmatrix} \mathrm{d}\tau$$

Making the substitution $x_s = a_s \cos(\tau-\phi_s)$, with $u_s = a_s \cos(\phi_s)$ and $v_s = a_s \sin(\phi_s)$; $a_s^2 = u_s^2 + v_s^2$, and $x_r = a_r \cos(\tau-\phi_r)$, with $u_r = a_r \cos(\phi_r)$ and $v_r = a_r \sin(\phi_r)$; $a_r^2 = u_r^2 + v_r^2$, we finally can write:

$$\int_0^{2\pi} \mu\overline{\omega}_{0F} \sum_{n=0}^{\infty} a_r^{2n+1} \cos(\tau-\phi_r)^{2n+1} \begin{Bmatrix} \cos(\tau) \\ \sin(\tau) \end{Bmatrix} \mathrm{d}\tau$$

where we have used

$$\frac{x}{1-x^2} = x \sum_{n=0}^{\infty} (x^2)^n$$

The last integral can be evaluated by making a change of variable $\tau-\phi_r=\alpha_r$ and using the following identities:

$$\cos^{2n+1}(\tau)=\sum_{k=0}^{n}a_{n,k}\cos((2n-2k-1)\tau)$$

and

$$\int_{-\phi_2}^{2\pi-\phi_2}\cos((2n-2k+1)\alpha_r)\begin{Bmatrix}\cos(\alpha_r)\\ \sin(\alpha_r)\end{Bmatrix}\mathrm{d}\alpha_r=\begin{Bmatrix}\pi\delta_{nk}\\ 0\end{Bmatrix}$$

Finally, we arrive at

$$\int_0^{2\pi}\mu\overline{\omega}_{0F}^2\frac{x_r}{1-x_r^2}\begin{Bmatrix}\cos(\tau)\\ \sin(\tau)\end{Bmatrix}\mathrm{d}\tau=\pi\mu\overline{\omega}_{0F}^2\frac{2}{\sqrt{1-a_r^2}+1-a_r^2}\begin{Bmatrix}u_r\\ v_r\end{Bmatrix}$$

where we have used

$$\sum_{n=0}^{\infty}\left(\frac{a_r^2}{4}\right)^n\binom{2n+1}{n}=\frac{2}{\sqrt{1-a_r^2}+1-a_r^2}$$

References

[1] H. Frahm, Device for damping vibrations of bodies, US Patent No. 989,958, 1911.
[2] R.A. Ibrahim, Recent advances in nonlinear passive vibration isolators, *Journal of Sound and Vibration* 314 (2008) 371–452.
[3] J.C. Snowdon, *Vibration and Shock in Damped Mechanical Systems*, John Wiley and Sons Inc., New York, 1968.
[4] M. Febbo, Optimal parameters and characteristics of a three degree of freedom dynamic vibration absorber, *Journal of Vibration and Acoustics* 134 (2012) 021010.
[5] N.A. Alexander, F. Schilder, Exploring the performance of a nonlinear tuned mass damper, *Journal of Sound and Vibration* 271 (2009) 15–24.
[6] M. Karyeaclis, T.K. Caughey, Stability of a semi-active impact damper, *Journal of Applied Mechanics* 56 (1989) 926–940.
[7] R.E. Roberson, Synthesis of a non-linear dynamic vibration absorber, *Journal of the Franklin Institute* 254 (1952) 205–220.
[8] L.A. Pipes, Analysis of a non-linear dynamic vibration absorber, *Journal of Applied Mechanics* 20 (1953) 515–518.
[9] A. Soom, M. Lee, Optimal design of linear and nonlinear vibration absorbers for damped systems, *Journal of Vibration and Acoustics, Stress Reliability Design* 105 (1983) 112–119.
[10] J.C. Nissen, K. Popp, B. Schmalhorst, Optimization of a non-linear dynamic vibration absorber, *Journal of Sound and Vibration* 110 (1985) 149–154.
[11] H.J. Rice, Combination instability of the nonlinear vibration absorber, *Journal of Sound and Vibration* 108 (1986) 526–532.
[12] J. Shaw, S.T. Shaw, A.G. Haddow, On the response of the non-linear vibration absorber, *International Journal of Non-Linear Mechanics* 24 (4) (1989) 281–293.
[13] S. Natsiavas, Steady stated oscillations and stability of non-linear dynamic vibration absorbers, *Journal of Sound and Vibration* 156 (1992) 227–245.
[14] S.S. Oueini, A.H. Nayfeh, J.R. Pratt, A Nonlinear Vibration Absorber for Flexible Structures, *Nonlinear Dynamics* 15 (1998) 259–282.
[15] S.S. Oueini, C.M. Chin, A.H. Nayfeh, Dynamics of a Cubic Nonlinear Vibration Absorber, *Nonlinear Dynamics* 20 (1999) 283–295.
[16] S.J. Zhu, Y.F. Zheng, Y.M. Fu, Analysis of non-linear dynamics of a two-degree-of-freedom vibration system with non-linear damping and non-linear spring, *Journal of Sound and Vibration* 271 (2004) 15–24.
[17] E. Gourdon, N.A. Alexander, C.A. Taylor, C.H. Lamarque, S. Pernot, Nonlinear energy pumping under transient forcing with strongly nonlinear coupling: *theoretical and experimental results*, *Journal of Sound and Vibration* 300 (2007) 522–551.
[18] A.F. Vakakis, O.V. Gendelman, G. Kerschen, L.A. Bergman, M.D. McFarland, Y.S. Lee, *Nonlinear Targeted Energy Transfer in Mechanical and Structural Systems*, vols. I and II, Springer, 2009.
[19] G. Kerschen, Y.S. Lee, A.F. Vakakis, D.M. McFarland, L. Bergman, Irreversible passive energy transfer in coupled oscillators with essential nonlinearity, *SIAM Journal on Applied Mathematics* 66 (2006) 648–679.
[20] O.V. Gendelman, Targeted energy transfer in systems with non-polynomial nonlinearity, *Journal of Sound and Vibration* 315 (2008) 732–745.
[21] M. Febbo, A finite extensibility nonlinear oscillator, *Applied Mathematics and Computation* 217 (2011) 6464–6475.
[22] M. Febbo, Harmonic response of a class of finite extensibility nonlinear oscillators, *Physica Scripta* 83 (2011) 065009. (12 pp).
[23] M.A. Acar, C. Yilmaz, Design of an adaptive-passive dynamic vibration absorber composed of a string–mass system equipped with negative stiffness tension adjusting mechanism, *Journal of Sound and Vibration* 332 (2013) 231–245.
[24] T.D. Le, K.K. Ahn, A vibration isolation system in low frequency excitation region using negative stiffness structure for vehicle seat, *Journal of Sound and Vibration* 330 (2011) 6311–6335.
[25] J.J. Thomsen, *Vibrations and Stability*, Springer-Verlag, Berlin, 2010.
[26] A.H. Nayfeh, D.T. Mook, *Nonlinear Oscillations*, John Wiley and Sons, 1979.
[27] G. Gatti, M.J. Brennan, I. Kovacic, On the interaction of the responses at the resonance frequencies of a nonlinear two degrees-of-freedom system, *Physica D* 239 (2010) 591–599.
[28] D.T. Mook, N. HaQuang, R.H. Plaut, The influence of an internal resonance on nonlinear structural vibrations under combination resonance conditions, *Journal of Sound and Vibration* 104 (1986) 229–241.